Microstructural modulation and cellular uptake of high-aspect ratio gold nanotubes for phototherapy

Sunjie Ye[1,3#], Arsalan A Azad[2#], Joseph E Chambers[2], Alison J Beckett[4], Lucian Roach[1], Zabeada Aslam[5], Ian A. Prior[4], Alex F Markham[3], Louise P Coletta[3#], Stefan J Marciniak[2]* and Stephen Evans[1]*

[1] School of Physics and Astronomy, Woodhouse Lane, Leeds, LS2 9JT

[2] Cambridge Institute for Medical Research, Keith Peters Building, Hills Road, Cambridge, CB2 0XY

[3] Leeds Institute of Medical Research, St James's University Hospital, University of Leeds, Leeds, LS9 7TF, UK

[4]Institute of Translational Medicine, University of Liverpool, Crown Street, Liverpool, L69 3BX

[5]School of Chemical and Process Engineering, University of Leeds, Leeds, LS2 9JT, U.K.

KEY WORDS: gold nanotubes**,** gavlanic replacement, NIR absorption, intracellular trafficking, single particle tracking, cellular uptake

ABSTRACT

The application of nanomaterials for phototherapy depends on their possessing appropriate structural and surface properties for low cytotoxicity and efficient cellular uptake, as well as near-infrared (NIR) optical absorption for desirable photo-responses. Hence, the development of effective and safe phototherapy nanoagents will considerably benefit from the ability to fabricate nanostructures with tunable physicochemical features, and comprehensive understanding of cellular interactions with nanostructures. Here, we present the preparation of

gold nanotubes (AuNTs) with tailorable morphological, compositional and optical characteristics, via the adjustment of reaction conditions in the galvanic replacement. The modulation of optical properties allows the creation of AuNTs with strong NIR absorption. The surface modification renders the dispersibility of AuNTs in aqueous medium, along with low cytotoxicity. A series of *in vitro* experiments using primary mesothelioma cells was used to investigate the uptake dynamics and cellular fate of these gold nanotubes. Using correlative light and optical reflectance single particle tracking analysis, we demonstrate the active uptake and trafficking of AuNTs to the peri-nuclear region in mesothelioma cells. Confocal and 3D correlative light-electron microscopy demonstrate AuNTs to be confined initially within vesicles from which they escape at later time points. Our work has important implications for the controllable fabrication and cellular interactions of nanomaterials, and will enable rational design of nanoconstruct for phototherapy and drug delivery applications.

INTRODUCTION

Phototherapy offers the potential to target the killing of cancer cells whilst causing only minimal damage to normal tissues.[1-4] Typically near-infrared (NIR) light is used because of its superior tissue penetration. Photothermal therapy (PTT) makes use of photothermal conversion agents (PTCAs) that strongly absorb light which they convert into heat. This leads to rapid local heating and cell death.[5-7] PTT can be controlled spatiotemporally, thus avoiding damage to non-targeted regions,[8-10] but PTT alone is unlikely to kill all tumor cells, due to the limited tissue penetration depth of light and the nonuniform heat distribution. Combining PTT with other therapeutic modalities, such as chemotherapy and gene-therapy, can enhance therapeutic efficacy.[11-13] Consequently, there is much interest in engineering cooperative systems to achieve combined photothermal-chemo/gene therapy.[14-16] The uses of NIR-mediated PTCAs have been shown to exhibit synergistic effects between drugs (chemotherapeutic drugs or

therapeutic nucleic acids) and NIR irradiation.[17-20] However, most nanocarriers are internalised via endocytic pathways leading to the majority of the particles taken-up by cells residing within endosomes.[21-23] This often leads to modification of their optical absorbance properties due to agglomeration,[24] as well as reducing the efficacy of any therapeutic agents relaesed thus limiting the therapeutic benefit.[21] These limitations motivated studies into the cytosolic delivery of drug-loaded nanocarriers,[11, 25-26] for example via photothermal disruption of the endo/lysosomal membranes (ref). Recent studies have revealed that one-dimensional (1D) nanomaterials with lengths of several micrometers can enter cells via non-endocytic pathways.[27] We hypothesised that NIR-active nanocarriers with similar structural parameters might offer an alternative strategy for photothermally-triggered cytosolic drug delivery.

AuNTs represent an intriguing subset of 1D nanomaterials. Their accessible inner cavity can, in principle be loaded with drugs,[28-29] their open ends can be used as gates for controlled drug release,[30] and their lower heat capacity enables better pulse heating that is beneficial for photoacoustic imaging and photothermal therapy.[31] Despite the potential merits of gold nanotubes, their lack of NIR absorption and insufficient understanding of cellular interactions have hindered their exploitation. Indeed, Bi *et al* synthesised pentagonal AuNTs with uniform structures in large quantities, while the obtained AuNTs showed an absorption peak at 550 nm.[32] previous literature suggests that the large dimension along the longitudinal axes of the AuNTs (from several micrometre to tens of micrometres) might be an issue for cell-based applications.[33] Therefore, it is desired to develop a method for fabricating gold nanotubes with tailorable properties, and systematically investigate nanotube-cell interactions.

Here, we report a simple method for engineering AuNTs with tailorable optical properties, based on the change of microstrucutre though the gavlanic replacement between silver

nanowire and $HAuCl_4$, at room temperature. Energy-dispersive X-ray spectroscopic (EDX) mapping and compositional analysis were performed to elucidate the mechanism regarding the microstructral modulation. The control of optical properties allows the creation of AuNTS with absorption in NIR region, which have been modifed by thio-PEG-FITC to impart dispersablity and reduce cytotoxicity. Furthermore, A series of methodologies were used to investigate cellular uptake and subcellular fate of AuNTs, revealing their time dependent escape from intracellular membrane encapsulation to the cytosol.

RESULTS AND DISCUSSION

Template synthesis represents a general and powerful strategy for preparing gold hollow structures.[34] The synthesis through the galvanic replacement of Au precursors with Ag template provides a method for producing well-defined hollow structures with tailorable structural and optical properties, depending on the adjustment of the ratio of Au/Ag in the reaction system.[35-37] In this work, polyol synthesis has been adopted for the preparation of Ag nanowires (AgNWs), which function as templates for producing the AuNTs (Figure 1a). The protocol involves the introduction of a silver precursor solution ($AgNO_3$) and capping agent polyvinylpyrrolidone (PVP) into ethylence glycol (EG), which plays dual roles as both a reducing agent and solvent.[38] Ag nanowires were synthesised at a high wire-to-particle ratio, (Figure 1b and S1), and possess a diameter of 100±20 nm (Figure S2). These nanowires have a pentagonal cross-section (Inset of Figure 1b), arising from the uniaxial growth along the 5-fold axes of multiple-twinned seeds of Ag decahedra.[33, 38]

AuNTs were prepared via a room-temperature galvanic replacement of gold precursor ($HAuCl_4$) and sacrificial Ag nanowires, capitalising on the introduction of CTAB.[32] It is

generally acknowledged that the formation of hollow gold nanostructures via galvanic replacement needs high reaction temperatures to deliver well-defined morphology,[39] for example, 100°C for PVP-capped Ag nanowires with $HAuCl_4$.[40] CTAB plays essential roles in enabling the preparation of well-defined AuNTs via a room-temperature galvanic reaction, by dissolving AgCl solid and enhancing the inter-diffusion rate between Ag and Au.[39] In addition, CTAB molecules have preferential adsorption onto {100} facets which dominate the side surfaces Ag nanowires, thus leading to the selective deposition of $AuCl_4^-$ onto the side surfaces and eventually the formation of open-ended AuNTs.[32] Scanning electron microscopy (SEM) image of resultant AuNTs (synthesised with $HAuCl_4$ of 2× stoichiometric amounts) demonstrated well-defined tubular structures including an internal cavity, open ends and uniform walls (Figure 2b). Furthermore, these nanotubes assume structural attributes of Ag nanowires, e.g. five straight side edges with a pentagonal cross section (Inset of Figure 1c). In the transmission electron microscopy (TEM) image of an individual AuNT, the edges appear denser than the central portion owing to the hollow structure of the product. The thickness of the nanotube wall, as represented by the denser edge, is measured to be ~12 nm.

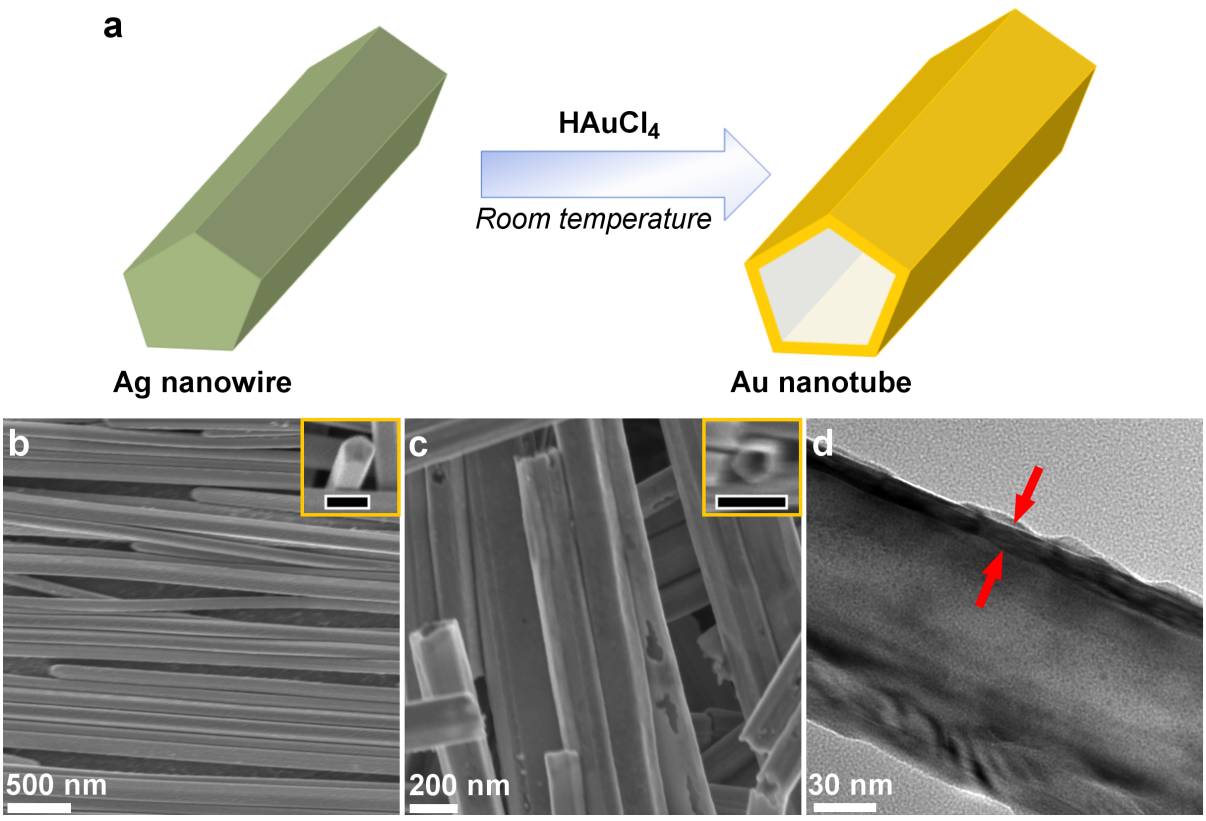

Figure 1. Preparation of AuNTs using Ag nanowires as templates: (a) schematic illustration of the reaction; (b) SEM image of Ag nanowires, with inset showing pentagonal cross section (Scale bar in inset: 200 nm); (c) SEM image of AuNTs (synthesised with $HAuCl_4$ of 2× stoichiometric amount), with inset showing pentagonal cross section (Scale bar in inset: 200 nm); (d) TEM image of an AuNT, with the dark edge showing the wall thickness (red arrows).

Intriguingly, we found that the morphology of the final AuNTs was largely dependent on the amount of $HAuCl_4$ added into the reaction system. At the stoichiometric amount of $HAuCl_4$, the products exhibit tubular structure with alternate darker and lighter banded regions on the wall. (Figure 2a and d). When the amount of $HAuCl_4$ was doubled, nanotubes displayed uniform and smooth walls (Figure 2b and e). When $HAuCl_4$ of 3× stoichiometric amount was used, the obtained tubular structures possessed pinholes associated with the walls and small

nanoparticles attached on the surface (Figure 2c and f). Fragmentation of the nanotube occurred to some extent, resulting the existence of discrete morphology. It is important to note that the structural evolution with the increased amount of $HAuCl_4$ appears to follow a pathway distinct from that for the reaction of PVP-capped Ag nanowires with $HAuCl_4$ at 100°C.[40]

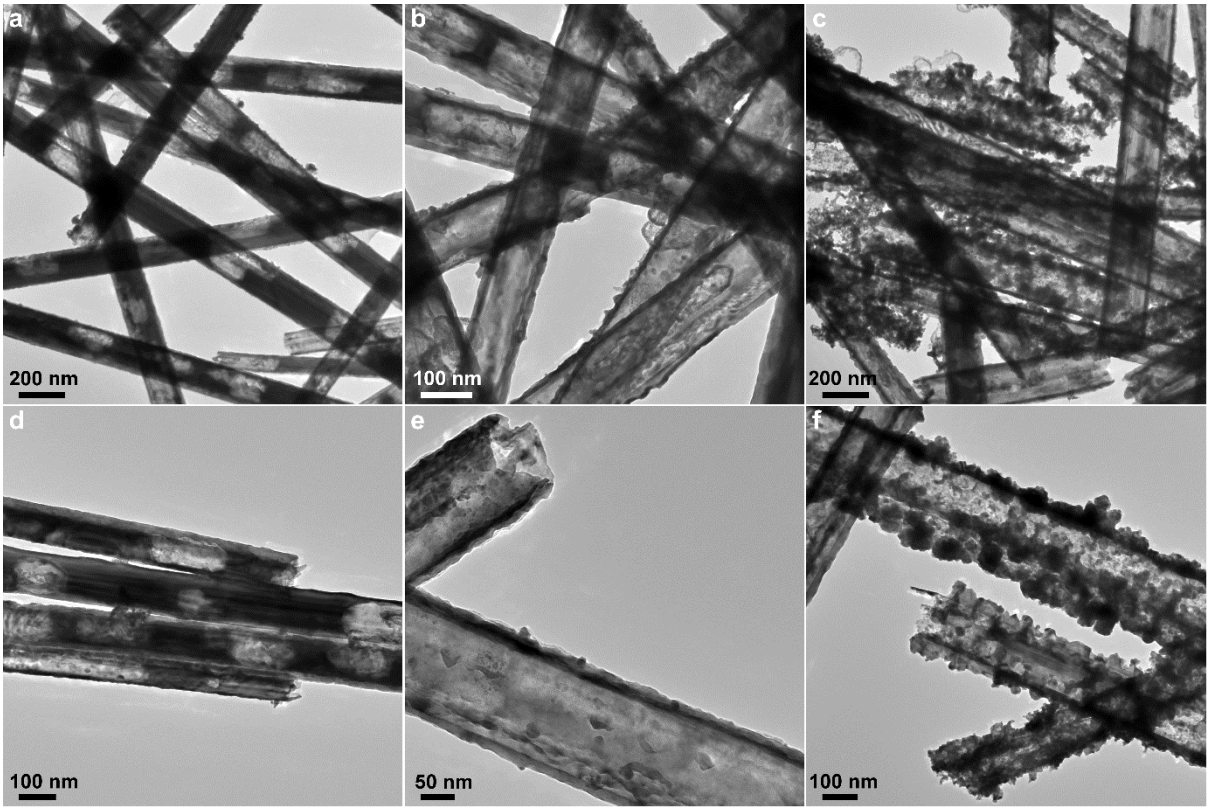

Figure 2. AuNTs prepared with varying $HAuCl_4$ amount demonstrate different microstructures. $HAuCl_4$ of stoichiometric amount (see experimental section): (a) Low- and (d) High-magnification TEM images; $HAuCl_4$ of 2× stoichiometric amount: (b) Low- and (e) High-magnification TEM images; $HAuCl_4$ of 3× stoichiometric amount: (c) Low- and (f) high-magnification TEM images. Scale bars shown in insets.

To better understand the mechanism of these observed differences in the microstructure of nanotubes we collected EDX elemental maps of the elemental distribution (Figure 3). For nanotubes synthesised with the stoichiometric amount of $HAuCl_4$, the map of Au element shows a homogenous and seamless layer (Figure 3a). Conversely, that for the Ag element shows regions of negligible contrast in agreement with the dark areas in the high-angle annular dark-field scanning transmission electron microscopic (HAADF-STEM) image, which correspond to the vacancies of Ag element. Notably, the overlay of Au and Ag suggests a clear profile of Au element along the tubular structure, indicating the epitaxial deposition of gold atoms on the surfaces of silver template. The nanotubes synthesised with $HAuCl_4$ of 2× stoichiometric amount manifest uniformity in HAADF-STEM image, as well as maps of Au and Ag elements (Figure 3b). A good co-location of Au and Ag is observed in the overlay image, revealing the nanotube wall is composed of Au-Ag alloy. The HAADF-STEM image, Au and Ag element maps of an individual nanotube synthesised with $HAuCl_4$ of 3× stoichiometric amount all demonstrate structures having rough surfaces coupled with pores in the wall of irregular shapes and sizes (Figure 3c). The overlay image shows the convergence of Au and Ag signals, with no phase segregation observed either for the nanotube wall or small nanoparticles attached on the surface, which indicates Au are Ag are present in the form of alloy.

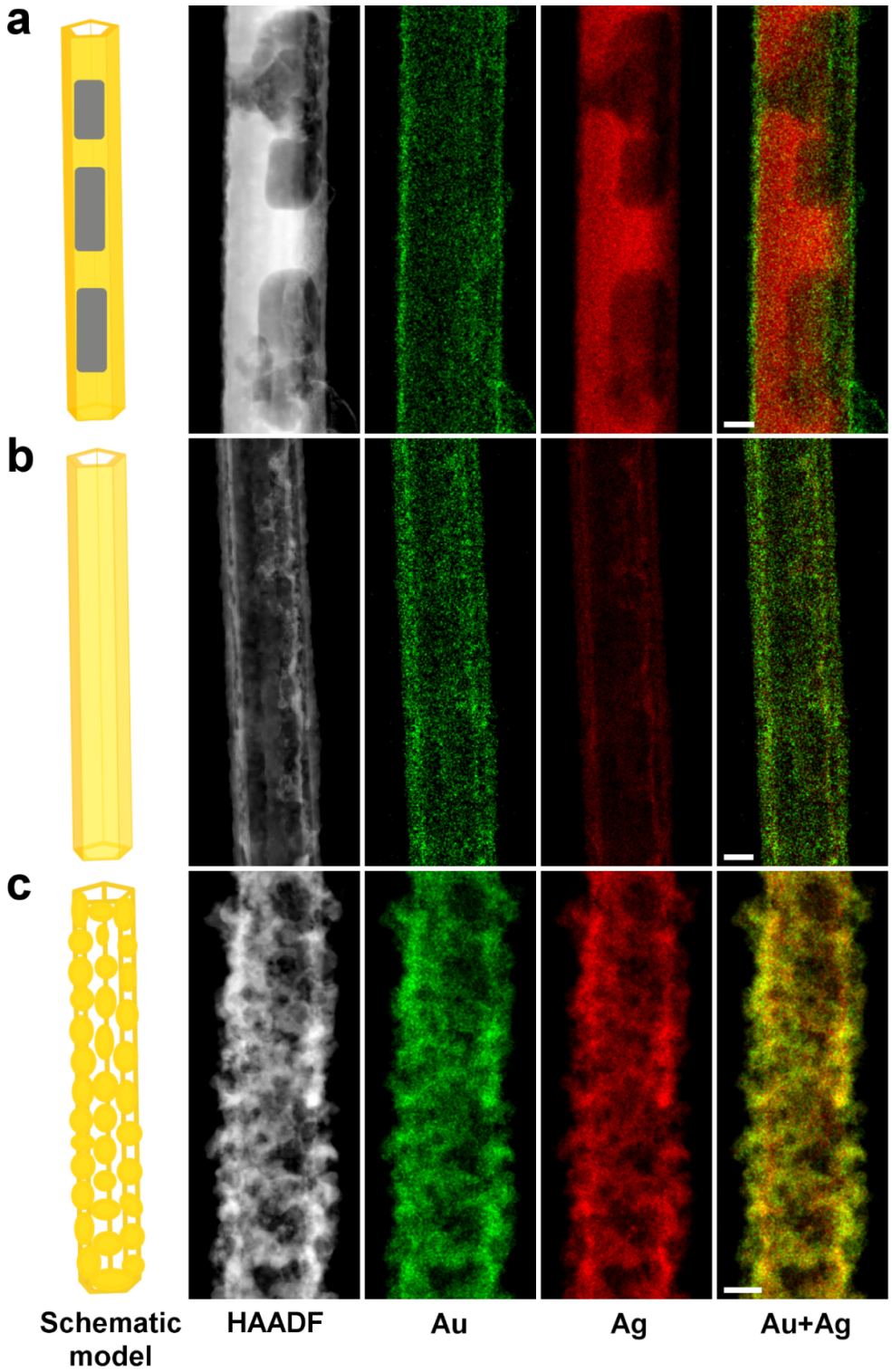

Figure 3. AuNTs prepared with varying $HAuCl_4$ amount exhibit different patterns of compositional distribution. Schematic model, HAADF image and EDX mapping of AuNTs synthesized with $HAuCl_4$ of (a) stoichiometric amount; (b) 2× stoichiometric amount; (c) 3× stoichiometric amount. All scale bars represent 50 nm.

We also conducted AAS measurements of nanotube dispersions to investigate the compositional variation of nanotubes synthesised with varying $HAuCl_4$ amounts. In all cases examined, nanotubes were composited of Au and Ag. The mass percentage of Au increases with the rise of $HAuCl_4$ amounts in the range from 1x to 2x stoichiometric amount, and exhibits a quasi-plateau in the range from 2x to 3x stoichiometric amount. The EDX and atomic absorption spectroscopy (AAS) results together enabled us to elucidate the formation mechanism and identify the reaction pathway for each sample depicted in Figure 2.

It is noteworthy that, Sun *et al* previously conducted a comprehensive mechanistic study on the replacement reaction between $HAuCl_4$ and PVP-capped silver nanostructures at 100°C, via the titration of silver nanostructures with a $HAuCl_4$ solution, with varying volumes of the $HAuCl_4$ solution (1 mM).[40] Our work, by contrast, focusses on the replacement reaction at room temperature, and highlights the modulation of the microstructure by altering the $HAuCl_4$ amount added all at once into the reaction system.

With the addition of $HAuCl_4$ at stoichiometric amount, the reaction proceeds in two distinct steps: (I) The displacement between Ag and $AuCl_4^-$ ions initially produces Au atoms that form patches on the surface of the silver template via epitaxial deposition, owing to the good lattice matting between and Au and Ag. (FCC crystalline structures for Au and Ag, with a lattice constant 4.0786Å for Au, and 4.0862 for Ag). (II) A corrosion process follows with the oxidation of Ag acting as the anode reaction to provide electrons that migrate to the uncovered surface of the Ag nanowire thereby reducing $AuCl_4^-$ into Au atoms (cathode reaction). As a result, an intact Au layer was formed with Ag voids present at the initial reaction sites, creating a tube-like structure with partially hollow cavity (Figure 2a and 3a).[39]

In the system with $HAuCl_4$ 2× stoichiometric amount, the reaction first follows the pathway described in step (I). Higher $HAuCl_4$ concentration facilitates the diffusion of $AuCl_4^-$ ions in the solution into as-formed volume defects of Ag template to reach the newly formed Ag surface. The etching of the Ag template via the replacement continues and enlarges the inner cavity. In conjunction with this process, alloying takes place between the epitaxially-deposited Au coating and covered Ag surface, due to the larger stability of homogenous Au-Ag than that of either pristine Au or Ag. The combination of etching and alloying leads to the formation of the nanotubes with a uniform wall of Au-Ag alloy wall and well-defined inner cavity (Figure 2b and 3b).

When $HAuCl_4$ 3× stoichiometric amount is added, the additional $HAuCl_4$ can selectively etch Ag atoms in the Au-Ag alloy wall, resulting in a dealloying process. Previous reports showed that this dealloying process alters the mass percentage of Au (Au%) in the nanotube to ca. 90% and produces large pores (Size > 20 nm) on the wall.[33, 40] Intriguingly, in the present work, the Au% plateaued at approximately 60% from 2x stoichiometric amount onwards (Figure 4a). This suggests a lack of a pronounced dealloying, which is also evidenced by the observation of homogenous Au-Ag alloy without elemental segregation (Figure 3c). This difference in the extent of dealloying may be caused by the enhanced energy barrier of dealloying at the room temperature in comparison with that at 100°C. Therefore, we suggest that, the pores in the nanotube wall (Figure 2c and 3c) may result from the morphologies reconstruction following a modest dealloying process.

The tailoring of the microstructure and composition enables the control of the optical properties of resultant AuNTs. UV-visible spectra were collected from nanotubes with different Au% (31.6%, 44.3%, 59.0% and 62.3%, synthesized with Au amount of 1x, 1.5x, 2.0x and 3.0x

stoichiometric amount, respectively) (Figure 4b). All spectra showed peaks (shoulder peak for Au%=44.3) around 450 nm, due to the existence of Ag. Comparisons were performed for the dominant peak in the wavelength of range of 600 nm and 1000 nm, which has been assigned to the transverse plasmon band of Au-Ag tubular nanostructures (Figure 4c). This peak shows a red shift from 620 nm to 926 nm, with an increase of Au% from 31.6% to 59.0%. The peak shift is mainly ascribable to the enlargement of the inner cavity, corresponding to the microstructural evolution from partially hollow morphology to the well-defined nanotube structure (Figure 2a and 3a). When Au composition is increased to 62.3%, a blue-shift to 700 nm is observed, accompanied by the appearance of a new peak around 550 nm. These spectral changes may arise from the fragmentation of nanotubes, the emergence of Au-Ag alloy nanoparticles on the nanotube surface, as well as the coupling between nanoparticles and nanotube wall. Taken together, AuNTs synthesized with 2× stoichiometric amount exhibit extinction band well-located in NIR tissue window (650 nm - 950 nm), hence having be used for the following surface modification and *in vitro* cell study.

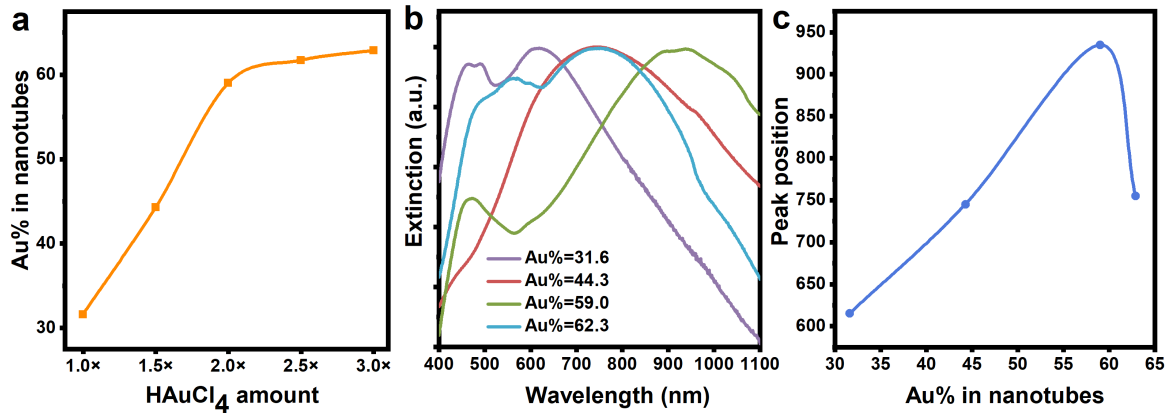

Figure 4. Synthesis of AuNTs with varying $HAuCl_4$ amount leading to the modulation of optical properties. (a) Plot of Au% in nanotubes (measured by AAS) Vs $HAuCl_4$ amount relative to stoichiometric amount; (b) UV-vis spectra of AuNTs with different Au% in nanotubes. (c) Plot of the position of dominant peak with Au% in nanotubes (determined by AAS)

Although CTAB plays an essential role in obtaining well-defined AuNTs at room temperature, the resulting CTAB-AuNTs were prone to severe agglomeration in Mill-Q (Figure S3). Moreover, although the concentration of CTAB required in our protocol is much lower than that of conventional CTAB-mediated seed synthesis of gold nanorods (5 mM vs 100 mM),[41] even low levels of free CTAB are highly cytotoxic and would potentially reduce the biocompatibility of our AuNTs.[42, 43] To resolve the issues of aqueous dispersibility and CTAB toxicity, we carried out surface modification using Thiol-PEG-FITC. Confocal microscopy image of AuNTs after surface modification showed excellent correlation between fluorescence signal and gold nanotubes, confirming the successful conjugation of Thiol-PEG-FITC. (Figure 5a). Individual nanotubes can be resolved clearly, confirming good dispersibility of FITC-labelled AuNTs in aqueous medium. Examination of 100 FITC-AuNTs demonstrates a length of (10.1±3.9) μm. (Figure S4)

Next, we evaluated the cytotoxicity of FITC-AuNTs (Length: 10.1±3.9 μm, inner diameter: 100±20 nm, thickness: ~12 nm, Au%= 59.9%, aspect ratio: ~80) in primary mesothelioma cells.[44] Malignant mesothelioma is an incurable cancer of the mesothelium caused by exposure to the mineral asbestos.[45] With current standard care, the median survival with mesothelioma is approximately one year and so there is an important unmet need for novel targeted therapies. When FITC-AuNTs were incubated for 6 and 18 hours at 5 μg/ml and 25 μg/ml with adherent mesothelioma cells no significant cytotoxicity was observed (Figure 5b).

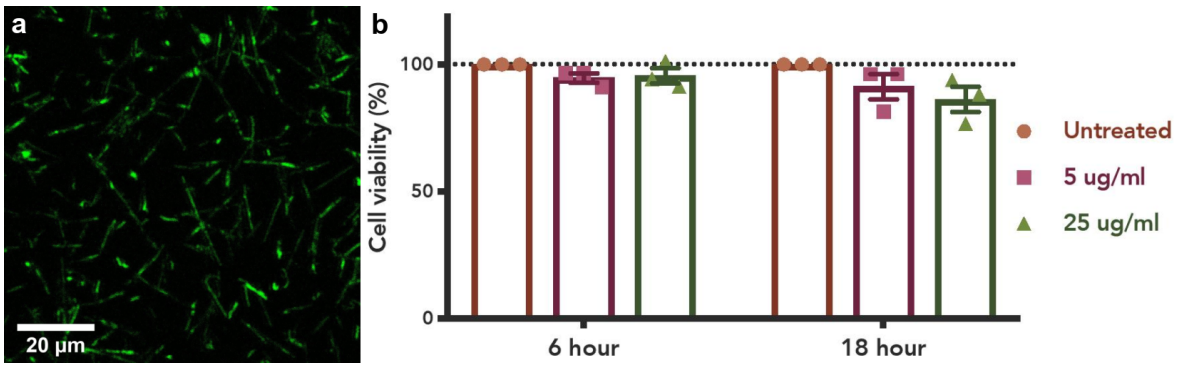

Figure 5. Surface functionalisation and cytotoxicity of AuNTs in mesothelioma cells. (a) A representative confocal microscopy image of AuNTs after surface modification using Thiol-peg-FTIC (Ex: 495 nm, Em: 520 nm; Scale bar: 20 µm). (b) Cytotoxicity of MESO 7T cells incubated at different concentrations of FITC-AuNTs ((Length: 10.1±3.9 μm, inner diameter: 100±20 nm, thickness: ~12 nm, Au%= 59.9) for 6 and 18 hours. Viability was measured using the CCK-8 assay (n=3).

Having established that FITC-AuNTs had appropriate physical, optical and cytotoxicity attributes to serve as PTCAs, we then examined their interaction with primary mesothelioma cells (Meso-7T; MesobanK, UK). Mesothelioma cells were plated at 20% confluence and cultured for 24 hours, then AuNTs were added after sonication for 10 seconds to prevent agglomeration. Time-lapse movies were acquired over 4 hours from the point of AuNT addition (Δt=30 s, total frames=480) and AuNTs were visualised using optical reflectance (Figure 6).[27, 46] Dynamics of the AuNTs were analysed by single-particle tracking.

To determine if AuNTs were actively trafficked within mesothelioma cells, a threshold of maximal track speed and track length displacements were used to identify active AuNT uptake events. Of all identifiable tracks, 80% (n=221) were above previously reported maximal track speeds for active-uptake events, for similar aspect ratio nanoparticles (0.1 µm/sec[27]) (Figure

6a). To obtain robust data, from these 221 tracks we chose those with track length displacements of at least 10 µm (Figure 6b), which is 10% of the diameter of a typical mesothelioma cell (99.5 ± 22.6 µm, n=20 cells, Table 1). A typical AuNT track trajectory is shown (Figure 6c and 6d). AuNT transport displayed the characteristic three stage uptake mobility as has been seen for the active transport of other nanoparticles [27]: (Stage I) low motility as AuNTs bind to the cell surface; (Stage II) high-velocity linear movement as AuNTs are transported actively; (Stage III) low-motility movement at the peri-nuclear region (Figure 6d and Supplementary Video S1).

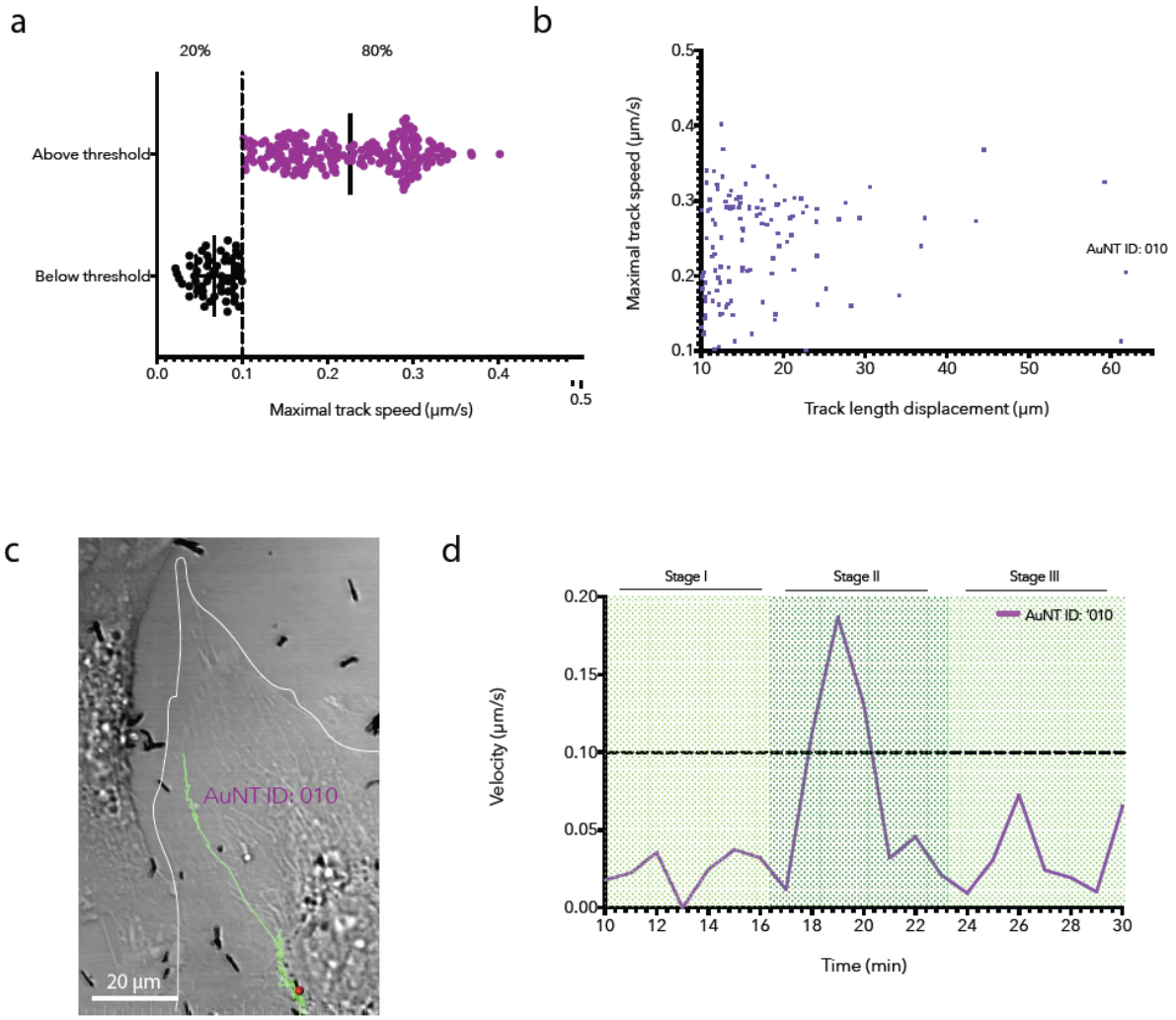

Figure 6. Live cell single-particle tracking of AuNTs in mesothelioma cells. Live-cell uptake of AuNTs in primary mesothelioma (Meso-7T) cells were visualised continuously for 4 hours post-AuNT incubation (Δt=30 s, total frames=480). (a) 80% (n=221) of all identifiable tracks were deemed above the published maximal track speed threshold for nanoparticle active uptake events (0.1 μm/sec[27]). (b) Scatter plot of the 221 maximal track speeds and track length displacement of 10 μm above was then used to identify fast-moving particles traversing over 1/10th of the average Meso-7T cell diameter (99.5 ± 22.6 μm, n=20 cells, Table 1). (c) Full length track trajectory of the AuNT 010 uptake into a Meso-7T cell. Scale bar represents 20 μm. (d) AuNT 010 transport displays characteristic three stage uptake mobility: (Stage I) low motility movement representing AuNT bound to the surface of the cell; (Stage II) high-motility linear-trajectory movement representing AuNT vesicular confinement and active transport to the peri-nuclear region (see Video S1); (Stage III) low-motility movement either confined within an organelle or free in the cytosol at the peri-nuclear region.

We then sought to assess the subcellular fate of the AuNTs in mesothelioma cells. Using phalloidin to visualise the F-actin cytoskeleton as a whole-cell mask, intracellular AuNTs were localised predominantly in a perinuclear localisation after 18 hours (Figure 7a). Three-dimensional rendering and orthogonal (z-axis) sections confirmed that AuNT were intracellular (Figure 7b and Supplementary Video S2). Previous studies have variously localised nanoparticles to endosomes, lysosomes or the cytosol.[47-48] Co-localisation studies were performed by fluorescence confocal microscopy using markers for early endosomes (EEA1), early sorting endosomes (SNX1), recycling endosomes (TNFR) and lipid droplets (Bodipy) (Figure 7c-h). AuNTs demonstrated moderate but incomplete co-localisation with markers for lysosomes (LAMP1) and lysosomes/late endosomes (LAMP3) (Figure 7c-d).

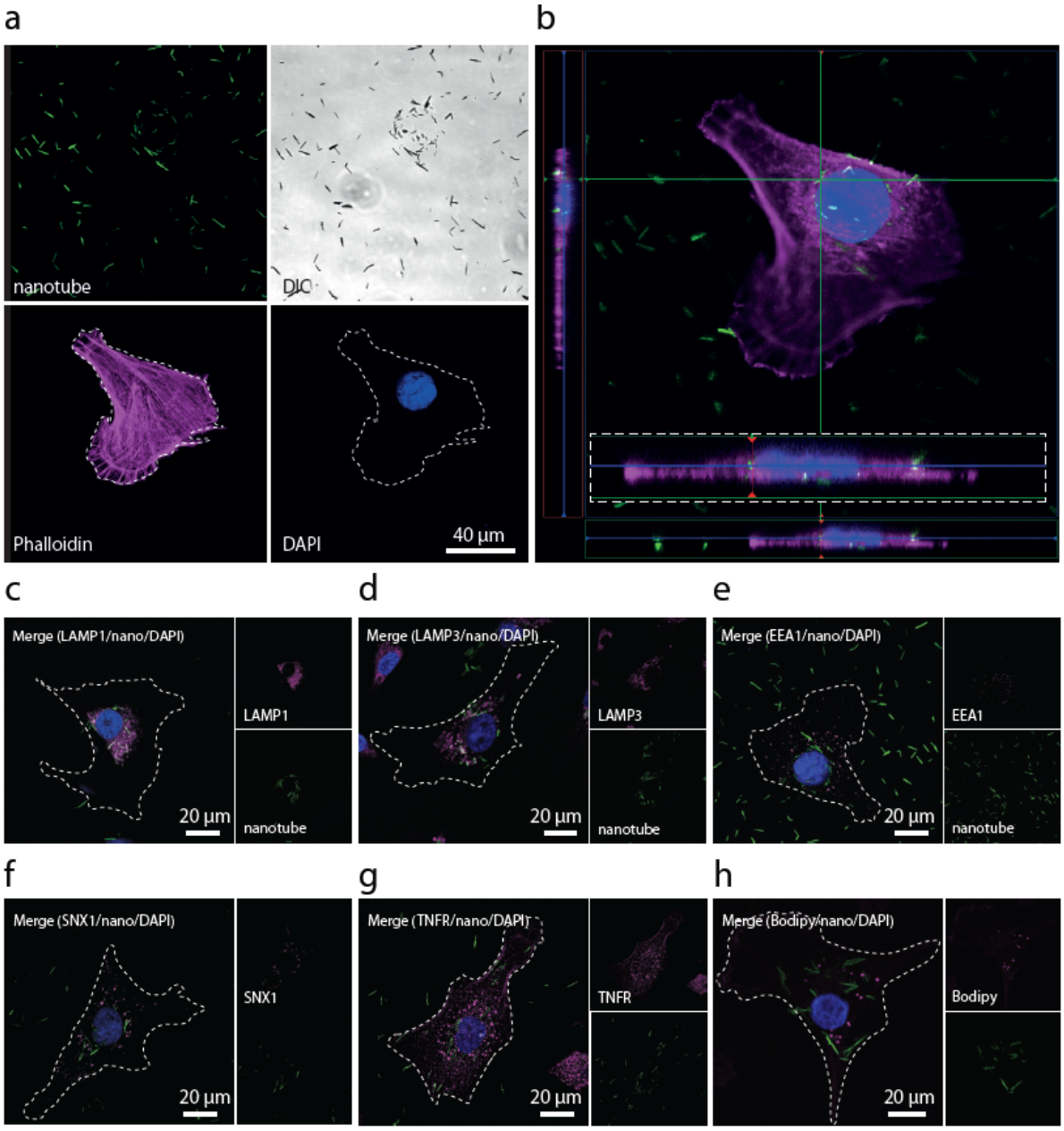

Figure 7 Subcellular fate of AuNTs in mesothelioma cells. (a) Confocal fluorescence image of a mesothelioma (Meso-7T) cell (phalloidin (cell mask), magenta: nuclei, blue: DIC)) demonstrating AuNT visualisation by optical scattering function (in green). Scale bar represents 40 µm. (b) Orthogonal slice demonstrating AuNT internalisation. (c-h) Localisation studies of AuNT with markers for: (c) lysosomes (LAMP1), (d) lysosome/late endosomes (LAMP3), (e) early endosomes (EEA1), (f) early sorting endosomes (SNX1), (g) recycling

endosomes (TNFR) and (h) lipid droplets (Bodipy). Nuclei stained with DAPI (blue). Scale bars represent 20 μm.

The imperfect co-localisation led us to suspect that at least some AuNTs were not confined within a single class of membrane-bound organelle and so we performed correlative light and electron microscopy (CLEM) of mesothelioma cells exposed to AuNTs for 6 or 18 hours**.** Cells containing AuNT were identified by live-cell confocal microscopy then and 60 nm slices were generated. At 6 hours following the addition, AuNT could be identified both free in the cytosol (Figure 8ai) and confined within vesicular structures (Figure 8aii and Figure S5). In contrast, by 18 hours, AuNT were found exclusively in the cytosol (Figure 8b). Taken together, these results demonstrate that AuNT are internalised and actively transported to the peri-nuclear region. At least a proportion of the AuNTs are initially endocytosed but after 18 hours have escaped the endosomal system to reside free in the cytosol.

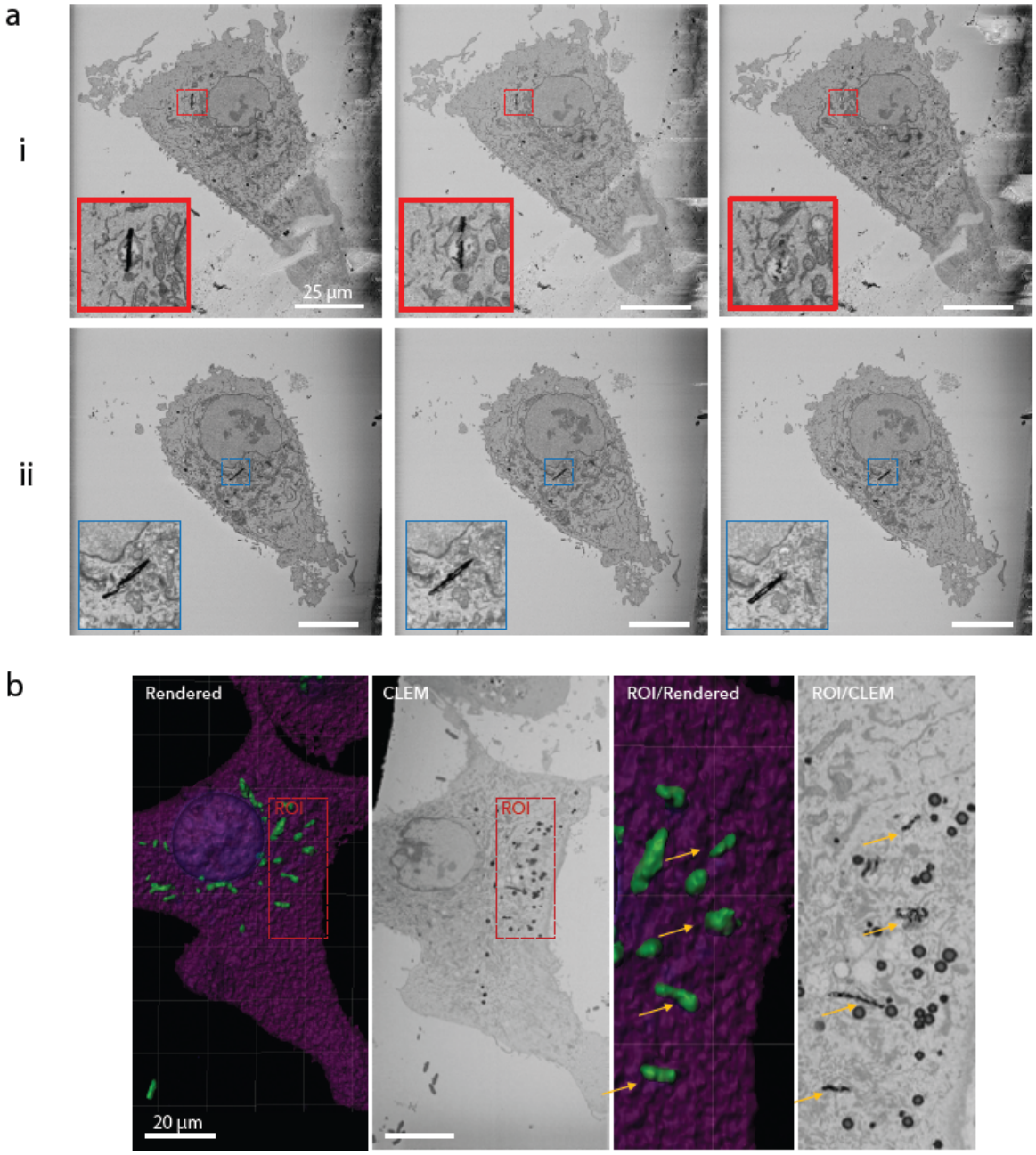

Figure 8 3D CLEM reveals AuNT vesicular confinement and escape in mesothelioma cells. 3D correlative light electron microscopy (CLEM) was used to determine the subcellular localisation of Au-nanotubes in Meso 7T cells at (a) 6 and (b) 18 hours, respectively. (a) At 6 hours AuNTs demonstrate a mixed distribution, both (a (i)) confined within vesicles and (a(ii)) freely distributed in cytosol. Bottom left insets show higher magnification of AuNTs of interest. Scale bars represent 25 µm. (b) At 18 hours all AuNTs are freely located within the cytosol.

The yellow arrowheads indicate the AuNTs visible in the corresponding EM slice shown in the enlarged region of interest (ROI). Scale bars represent 20 μm.

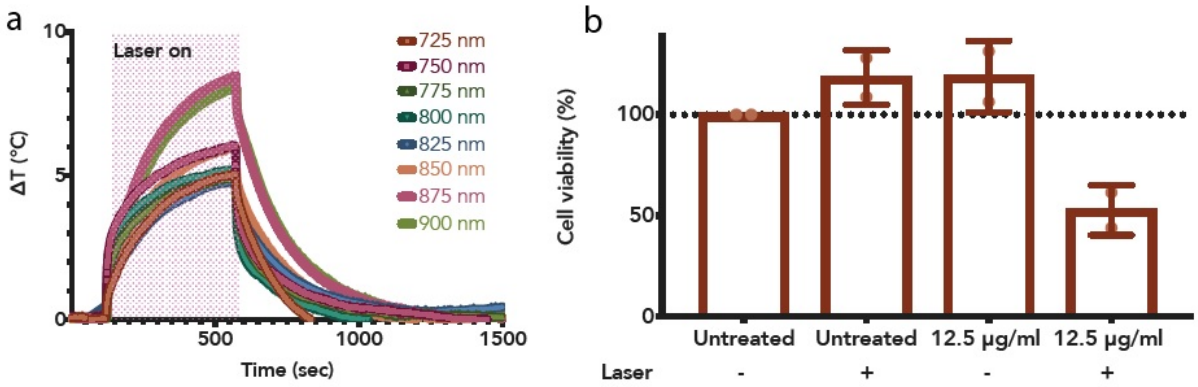

Figure 9 Photothermal effect of AuNTs: (a) Heating curves of FITC-AuNTs (25 μg/mL) in Milli-Q water, following laser irradiations at different wavelengths (Irradiation duration: 7.5 min; laser intensity: 1.9W/cm^3); (b) Cell viability after laser exposure: Meso 7T cells were cultured in the medium containing no AuNTs and AuNTs (12.5 μg/mL) and then irradiated with laser (Wavelength: 875 nm, exposure duration: 10 min for each well, laser intensity: 1.9W/cm^3) Cells in the absence of FITC-AuNTs without laser exposure were used as the control group. Results are shown as mean ±SD (2 technical replicates)

Encouraged by the NIR absorption, negligible cytotoxicity, and cellular internalisation of AuNTs, we tested the potential use of them as PTCAs. First, we evaluated their photothermal effects in aqueous medium (Milli-Q) as a function of time, during the irradiation with a continuous wave (CW) laser of different wavelength, at a power density of 1.9 W/cm^2 for 7.5 mins (Figure 9a). All temperature-time curves displayed a gradual temperature rise, indicative of heat transfer from AuNTs to the solution. The temperature rise is wavelength-dependent and varies from 4.8 to 8.5°C, which would lead to a temperature valid for hyperthermia treatments of cancer therapy (41 to 48°C) based on the body temperature of 37°C (25030381). The largest temperature change (Δ8.5°C) occurred under the irradiation of 875 nm laser, and thus 875 nm

was selected for the *in vitro* assessment of photothermal cell ablation.[49] The photothermal cytotoxicity of AuNTs was evaluated by exposing mesothelioma cells to a CW laser of 875 nm at a laser density of 1.9 W/cm2 for 10 mins. (Figure 9b). The laser irradiation alone did not cause cell death, while with the addition of AuNTs (12.5 μg mL^{-1}), the cell viability upon laser exposure decreased to 58.5±10.2 % (Figure 9b). These results reveal that AuNTs in combination with NIR laser irradiation can induce photothermal killing of cancer cells with low dosage of Au NTs. The observed photothermal effect and cytosol distribution of AuNTs provide the applicability for photothermally-triggered cytosol delivery towards combined photothermal-chemo/gene therapy.

CONCLUSIONS

We have developed an approach to synthesise microstructure-tunable AuNTs, by varying the amount of gold precursor introduced into the galvanic replacement of Ag nanowire template. The study using combined EDX mapping and compositional analysis reveals distinct reaction pathways for different gold precursor concentrations, providing further useful implications of room-temperature galvanic replacement. In addition, this approach can be used to construct hollow nanostructures of desirable structural, compositional and optical properties. Consequently, we have engineered NIR-absorbing AuNTs as PTCAs with a broad range of potential application including photothermal cancer therapy and photothermally-triggered drug release. Modification of AuNTs by thiol-PEG-FITC ensured dispersibility in aqueous medium with low cytotoxicity. The AuNTs were taken up by primary mesothelioma cells and actively transported to the peri-nuclear region where they eventually escaped vesicular confinement to reside free in the cytosol. The NIR absorption and cytosolic distribution of these nanotubes endow them with the potential to be engineered as photothermally-triggered non-viral cytosol

delivery vector for therapeutic molecules, to realize combined photothermal-chemo/gene therapy. We will explore the capability of our AuNTs for these uses in future work.

EXPERIMENTAL METHODS

Materials: Gold (III) chloride trihydrate (520918), cetyltrimethylammonium bromide (CTAB, H6269), Copper (II) chloride ($CuCl_2$, 203149), sulphuric acid (07208) and ammonium hydroxide solution (NH_3 in H_2O) were purchased from Sigma-Aldrich. Silver nitrate (11414), Polyvinylpyrrolidone (PVP, average M.W. 58,000, A14315) were purchased from Alfa Aesar. Fluorescein PEG Thiol, (FITC-PEG-SH, PG2-FCTH-3k, 3400Da) was purchased from NanoCS. Ethylene Glycol (EG, 10011073), hydrochloric acid (37%, UN1789) and nitric acid (70%, UN2031) and hydrogen peroxide (H/1750/17) were purchased from Fisher Scientific. Acetone (20066) was ordered from VWR. Milli-Q water (18.2 MΩ·cm at 25°C) was used. All chemicals were used without further purification.

Characterizations: The UV-Vis absorption spectra were recorded with a Perkin-Elmer Model Lambda35 spectrophotometer. SEM micrographs were obtained using a Hitachi SU8230 at a voltage of 2kV. Each SEM sample was prepared by placing 5 μL Ag NW or Au NT dispersion (in Milli-Q) onto an aluminium substrate and drying under room temperature naturally. TEM images and energy dispersive X-ray spectroscopy (EDX) mapping results were collected using a range of microscopes at the University of Leeds, a Tecnai F20 TEM/STEM operated at an accelerating voltage of 200 kV, and a Gatan Orius CCD camera running Digital Micrograph software, FEI Titan Themis 300 operated at 300kV fitted with high brightness X-FEG and Supertwin objective lens and a Super-X EDX system with windowless 4-detector design for

EDS mapping. (Bright field TEM images were collected with a Gatan OneView 16 Megapixel CMOS digital camera). To prepare samples for TEM imaging, 2 μL AuNT dispersion (in Milli-Q) was dropped onto a carbon-coated copper grid (Agar Scientific Ltd) and dried at room temperature naturally. To measure the elemetal Au and Ag contents in the Au NT sample, 200 μL Au NT dispersion was digested in 800 μL aqua regia, diluted with Milli-Q water to 10 mL, and analyzed using using an atomic absorption spectrometer. Confocal microscopy image of FITC-AuNTs (Figure 5a) was collected with a Zeiss LSM880+Inverted/Upright with Airyscan and Leica DM/SP8 Laser Scanning Confocal Microscope. (Ex: 495 nm; Em: 520 nm)

Reaction Preparation: Flasks, vials and stir bars were cleaned with aqua regia (nitric acid and hydrochloric acid in a volume ratio of 1:3) thoroughly rinsed with DI water, and dried in an 80ºC oven before use. Once dry, the flask and vials were allowed to cool to room temperature before use.

Synthesis of Ag NWs: For a typical synthesis, 10 mL of EG was added to round-bottom flask to which a stir bar was added. The flask was then suspended in an oil bath (temperature 152 ºC) and heated for 1 h under magnetic stirring (260 rpm). Concurrent to this heating, reagent solutions were prepared. After 1h heating, $CuCl_2$ solution in EG (4 mM, 80 μL) was injected into heated EG. The solution was then heated for another 15 min. 3 mL of PVP solution in EG (150 mM, concentration was calculated according to the repeating unit) was then injected into the heated EG, followed by $AgNO_3$ solution in EG (94 mM, 3mL). The reaction was allowed to last for 100 min, and then queched by cooling the reaction flask in a room temperature water bath. Products were then washed with acetone for 3 times by centrigugation (100g* 3 min) and Milli-Q water for 3 times (1000g* 5 min). The Ag NW pellet was re-dispersed in 5 mL Milli-Q for future use.

Formation of Au NTs: 1 mL of prepared Ag NW (concentration: 2.5mg/mL) was mixed with CTAB aqueous solution (20 mM, 2 mL), and then sonicated for 15 mins. $HAuCl_4$ aqueous solution (difference volume, 10 mM) was slowly added dropwise to the CTAB-Ag NW solution. The stoichiometric amount corresponds to 500 μL of 10 mM $HAuCl_4$ aqueous solution. The reaction was allowed to proceed at room temperature for 30min and magnetic stirring was used throughout the synthesis. The resultant solution was centrifuged at 1000 g for 3 mins and the supernatant was removed. The pellet was washed with CTAB aqueous solution (10 mM) and $NH_3{\cdot}H_2O$ (33%) subsequently, then redispersed in 200 μL $NH_3{\cdot}H_2O$ and kept for overnight to further remove the AgCl, according to reaction 1 (some Ag was also removed by treatment with $NH_3{\cdot}H_2O$, following reaction 2.[50]). The mixture was centrifuged (1000g, 2 min) and washed with CTAB aqueous solution (10 mM) twice. The final product of Au NTs was redispersed in Milli-Q.

$$AgCl\ (s) + 2NH_3{\cdot}H_2O \rightarrow [Ag(NH_3)_2]^+(aq) + Cl^-(aq) + 2H_2O \qquad (1)$$

$$4Ag\ (s) + 8NH_3(aq) + O_2 + 2H_2O \rightarrow 4[Ag(NH_3)_2]^+(aq) + 4OH^-(aq) \qquad (2)$$

Surface Modification with FITC-PEG-SH: the as-prepared Au NTs were added dropwise into the solution of (250 μL /mL) in a 1:1 volume ratio and allowed to react for overnight(magnetic stirring was used throughout the reaction) The Au NTs were then collected and wased by centrifugation (1500g*5 min)-redispersion (in Milli-Q) cycle for 3 times to remove free FITC-PEG-SH.

Cell culture: Primary mesothelioma cells (MESO-7T) were obtained from MesobanK (www.mesobank.com).[51] MESO-7T cells were authenticated by Short Tandem Repeat (*STR*) DNA profiling and then cultured in Roswell Park Memorial Institute (RPMI)-1640 growth

media supplemented with L-glutamine (2 mM), penicillin (100 U/ml), streptomycin (100 ug/ml), hEGF (20 ng/ml), hydrocortisone (1 μg/ml), heparin (2 μg/ml) and 10% FBS at 37°C and 5% CO_2.

AuNT uptake and subcellular localisation assays: MESO-7T cells were seeded at 80% confluence and cultured for a minimum of 24 hours. AuNTs were then sonicated for 10 seconds and added at a concentration of 25 μg/ml and incubated at 37°C and 5% CO_2 for 18 hours. After 18 hours, the cells were then washed for 3 x 1 minutes with PBS to remove residual AuNTs.

For immunofluorescence, cells were fixed in 4% paraformaldehyde and then permeabilised and blocked with 0.1% Triton X-100 in 2% BSA-PBS. Cell were then incubated with the following primary antibodies at the given dilution: 1:100 anti-LAMP1 (24170 Abcam), 1:100 anti-LAMP3 (HSB6), 1:100 anti-EEA1 (610457 BioLegend), 1:100 anti-SNX1 (995 Abcam), 1:100 anti-TNFR (82411 Abcam), Alex Fluor-568 Phalloidin (A-12380 Molecular Probes) and Bodipy (D3622). Cells were then washed 3 x 5 minutes with 1 x PBS and incubated with secondary antibodies Alexa-488, -568 and -647 goat anti-mouse or goat anti-rabbit obtained from Molecular Probes and used at a dilution of 1:400. Finally, cells were washed 3 x 5 minutes with 1 x PBS counterstained with DAPI and then mounted for confocal microscopy. AuNTs were visualised by optical scattering using reflectance confocal microscopy (RCM) as previously reported.[27]

Correlative light – electron microscopy: MESO-7T cells were plated onto 35mm gridded glass bottom microscopy dishes (MatTek) and treated with AuNTs The grid coordinates for suitable cells were identified by fluorescence microscopy. Cells were fixed and 60nm EM slices

(18x18nm resolution) were generated. Two-dimensional images were aligned and, were stated, 3D reconstructions created using Imaris software as described previously.[52]

Cells were fixed in 2.5% (w/v) glutaraldehyde in 0.1M phophate buffer (pH 7.4). Heavy metal staining comprised of reduced osmium (2% (w/v) OsO4 +1.5% (w/v) potassium ferrocyanide in ddH_2O), 1% (w/v) thiocarbohydrazide (w/v in ddH_2O), 2% OsO4 (w/v in ddH_2O), then 1% (w/v) aqueous uranyl acetate overnight at 4°C. The next day cells were finally stained with Walton's lead aspartate (0.02 M lead nitrate, 0.03 M aspartic acid, pH 5.5) at RT. To prevent precipitation artefacts the cells was washed copiously with ddH_2O between each staining step. Unless stated fixation and staining steps were performed in a Pelco Biowave®Pro (Ted Pella Inc. Redding California, USA) at 100w 20Hg, for 3 mins and 1min respectively. Dehydration was in a graded series of ethanol before filtration and embedding in hard premix resin (TAAB, Reading, UK).

Resin embedded cells were mounted onto cryo pins using conductive silver epoxy and targeted trimming was performed using an ultra-microtome (Leica, Milton Keynes, UK) as previously described.[53] The trimmed block was painted with Electrodag silver paint and coated with 10 nm AuPd using a Q150T sputter coater (Quorum Technologies). Cells were imaged using a Gatan 3View (Gatan, Pleasanton, USA) mounted on a Quanta 250 SEM (FEI, Hillsboro, Oregon, USA) at a resolution of 6 nm in x and y, 75nm in z. 3D reconstruction of the EM data was performed in Amira.

Single particle tracking: MESO-7T cells were seeded at 20% confluence on a 35mm live-cell images dishes (MatTek) and cultured for a minimum of 24 hours in regular growth medium. The dish was then mounted onto the Zeis LSM880 equipped with a live cell incubator and a 20X air objective lens to focus on the cell plane. AuNTs were sonicated for 10 seconds and then added at a concentration of 25 μg/ml and cell(s) and AuNT interaction were then

immediately imaged continuously for 4 hours (Δt=30 s, total frames=480). AuNTs were tracked using optical reflectance microscopy as previously reported.[27,46] Following acquisition 320 x 320 μm regions of interest were then cropped and batch analysed using a pre-written macro on Imaris 9.1.

Cytotoxicity assay: To assess cell viability, the formazan-based Cell counting kit-8 (CCK8) reporter assay kit was used according to the manufacturer's instructions (Sigma). In brief, MESO-7T cells were seeded at 5,000 cells per well in a 96-well plate and cultured for 24 hours. The cells were then incubated in a further 100 μl of growth medium containing the appropriate concentration of AuNTs for 6 or 18 hours. After incubation with AuNTs, cells were further incubated with 10 μl of sterile CCK-8 per well for 1 hour at 37 °C and 5 % CO_2. The optical density was then read for each well at 450 nm using a microplate spectrophotometer. Each experiment was done in triplicate, with three biological repeats.

AUTHOR INFORMATION

Corresponding Authors

*E-mail: s.d.evans@leeds.ac.uk

*E-mail: sjm20@cam.ac.uk

Author Contributions

S.Y. and A.A.A. contributed equally, and S.J.M. and S.D.E. are joint senior authors. S.Y. and A.A.A. designed experiments, performed a majority of experiments, analysed data, and wrote the manuscript. …… Z.A collected EDX mapping results and assisted in the analysis. L.R. collected heating curves and performed AAS measurements……

The authors declare no competing financial interest.

ACKNOWLEDGEMENT

SY and AAA were supported by a BLF-Papworth Fellowship from the British Lung Foundation and the Victor Dahdaleh Foundation. SJM is supported by the Medical Research Council, Cambridge BRC, Royal Papworth Hospital, and the Apha1-Foundation. SDE is supported by Health Services and Delivery Research Programme (MIC-2016-004). SDE, AFM, PLC wish to acknowledge support from the EPSRC (EP/EP/P023266/1). SY and AFM wish to acknowledge support from MRC (MR/L01629X).

REFERRENCES

(1) Cheng, L.; Wang, C.; Feng, L. Z.; Yang, K.; Liu, Z., Functional Nanomaterials for Phototherapies of Cancer. *Chem. Rev.* **2014**, 114 (21), 10869-10939

(2) Lal, S.; Clare, S. E.; Halas, N. J., Nanoshell-Enabled Photothermal Cancer Therapy: Impending Clinical Impact. *Acc. Chem. Res.* **2008**, 41 (12), 1842-1851.

(3) Chen, W. W.; Zhang, S. H.; Yu, Y. Y.; Zhang, H. S.; He, Q. J., Structural-Engineering Rationales of Gold Nanoparticles for Cancer Theranostics. *Adv. Mater.* **2016**, 28 (39), 8567-8585.

(4) Zhang, P. C.; Hu, C. H.; Ran, W.; Meng, J.; Yin, Q.; Li, Y. P., Recent Progress in Light-Triggered Nanotheranostics for Cancer Treatment. *Theranostics* **2016**, 6 (7), 948-968

(5) Jung, H. S.; Lee, J. H.; Kim, K.; Koo, S.; Verwilst, P.; Sessler, J. L.; Kang, C.; Kim, J. S., A Mitochondria-Targeted Cryptocyanine-Based Photothermogenic Photosensitizer. *J. Am. Chem. Soc.* **2017**, 139 (29), 9972-9978.

(6) Huang, X. H.; El-Sayed, I. H.; Qian, W.; El-Sayed, M. A., Cancer cell imaging and photothermal therapy in the near-infrared region by using gold nanorods. *J. Am. Chem. Soc.* **2006**, 128 (6), 2115-2120.

(7) Rastinehad, A. R.; Anastos, H.; Wajswol, E.; Winoker, J. S.; Sfakianos, J. P.; Doppalapudi, S. K.; Carrick, M. R.; Knauer, C. J.; Taouli, B.; Lewis, S. C.; Tewari, A. K.; Schwartz, J. A.; Canfield, S. E.; George, A. K.; West, J. L.; Halas, N. J., Gold nanoshell-localized photothermal ablation of prostate tumors in a clinical pilot device study. *Proc. Natl. Acad. Sci. U. S. A.* **2019**, 116 (37), 18590-18596.

(8) Choi, W. I.; Kim, J. Y.; Kang, C.; Byeon, C. C.; Kim, Y. H.; Tee, G., Tumor Regression In Vivo by Photothermal Therapy Based on Gold-Nanorod-Loaded, Functional Nanocarriers. *ACS Nano* **2011**, 5 (3), 1995-2003.

(9) Von Maltzahn, G.; Park, J. H.; Agrawal, A.; Bandaru, N. K.; Das, S. K.; Sailor, M. J.; Bhatia, S. N., Computationally Guided Photothermal Tumor Therapy Using Long-Circulating Gold Nanorod Antennas. *Cancer Res.* **2009**, 69 (9), 3892-3900.

(10) Goodman, A. M.; Neumann, O.; Norregaard, K.; Henderson, L.; Choi, M. R.; Clare, S. E.; Halas, N. J., Near-infrared remotely triggered drug-release strategies for cancer treatment. *Proc. Natl. Acad. Sci. U. S. A.* **2017**, 114 (47), 12419-12424.

(11) Kim, J.; Kim, J.; Jeong, C.; Kim, W. J., Synergistic nanomedicine by combined gene and photothermal therapy. *Adv. Drug Deliv. Rev.* **2016**, 98, 99-112.

(12) Melancon, M. P.; Zhou, M.; Li, C., Cancer Theranostics with Near-Infrared Light-Activatable Multimodal Nanoparticles. *Acc. Chem. Res.* 2011, 44 (10), 947-956.

(13) Fan, W. P.; Yung, B.; Huang, P.; Chen, X. Y., Nanotechnology for Multimodal Synergistic Cancer Therapy. *Chem. Rev.* **2017**, 117 (22), 13566-13638.

(14) Hembury, M.; Chiappini, C.; Bertazzo, S.; Kalber, T. L.; Drisko, G. L.; Ogunlade, O.; Walker-Samuel, S.; Krishna, K. S.; Jumeaux, C.; Beard, P.; Kumar, C.; Porter, A. E.; Lythgoe, M. F.; Boissiere, C.; Sanchez, C.; Stevens, M. M., Gold-silica quantum rattles for multimodal imaging and therapy. *Proc. Natl. Acad. Sci. U. S. A.* **2015**, 112 (7), 1959-1964.

(15) Sun, M. M.; Guo, J. W.; Hao, H. J.; Tong, T.; Wang, K.; Gao, W. P., Tumour-homing chimeric polypeptide-conjugated polypyrrole nanoparticles for imaging-guided synergistic photothermal and chemical therapy of cancer. *Theranostics* **2018**, 8 (10), 2634-2645.

(16) Son, S.; Nam, J.; Kim, J.; Kim, S.; Kim, W. J., i-Motif-Driven Au Nanomachines in Programmed siRNA Delivery for Gene-Silencing and Photothermal Ablation. *ACS Nano* **2014**, 8 (6), 5574-5584.

(17) Zhang, W.; Guo, Z. Y.; Huang, D. Q.; Liu, Z. M.; Guo, X.; Zhong, H. Q., Synergistic effect of chemo-photothermal therapy using PEGylated graphene oxide. *Biomaterials* **2011**, 32 (33), 8555-8561.
(18) Shen, J. L.; Kim, H. C.; Mu, C. F.; Gentile, E.; Mai, J. H.; Wolfram, J.; Ji, L. N.; Ferrari, M.; Mao, Z. W.; Shen, H. F., Multifunctional Gold Nanorods for siRNA Gene Silencing and Photothermal Therapy. *Adv. Healthc. Mater. Adv. Healthc. Mater.* **2014**, 3 (10), 1629-1637.
(19) Wei, P.; Chen, J. W.; Hu, Y.; Li, X.; Wang, H.; Shen, M. W.; Shi, X. Y., Dendrimer-Stabilized Gold Nanostars as a Multifunctional Theranostic Nanoplatform for CT Imaging, Photothermal Therapy, and Gene Silencing of Tumors. *Adv. Healthc. Mater.* **2016**, 5 (24), 3203-3213.
(20) Wang, B. K.; Yu, X. F.; Wang, J. H.; Li, Z. B.; Li, P. H.; Wang, H. Y.; Song, L.; Chu, P. K.; Li, C. Z., Gold-nanorods-siRNA nanoplex for improved photothermal therapy by gene silencing. *Biomaterials* **2016**, 78, 27-39.
(21) Stewart, M. P.; Sharei, A.; Ding, X. Y.; Sahay, G.; Langer, R.; Jensen, K. F., In vitro and ex vivo strategies for intracellular delivery. *Nature* **2016**, 538 (7624), 183-192.
(22) Lee, J.; Sharei, A.; Sim, W. Y.; Adamo, A.; Langer, R.; Jensen, K. F.; Bawendi, M. G., Nonendocytic Delivery of Functional Engineered Nanoparticles into the Cytoplasm of Live Cells Using a Novel, High-Throughput Microfluidic Device. *Nano Lett.* **2012**, 12 (12), 6322-6327.
(23) Verma, A.; Uzun, O.; Hu, Y. H.; Hu, Y.; Han, H. S.; Watson, N.; Chen, S. L.; Irvine, D. J.; Stellacci, F., Surface-structure-regulated cell-membrane penetration by monolayer-protected nanoparticles. *Nat. Mater.* **2008**, 7 (7), 588-595.
(24) Comenge, J.; Fragueiro, O.; Sharkey, J.; Taylor, A.; Held, M.; Burton, N. C.; Park, B. K.; Wilm, B.; Murray, P.; Brust, M.; Levy, R., Preventing Plasmon Coupling between Gold Nanorods Improves the Sensitivity of Photoacoustic Detection of Labeled Stem Cells in Vivo. *ACS Nano* **2016**, 10 (7), 7106-7116.
(25) Kim, H.; Lee, D.; Kim, J.; Kim, T. I.; Kim, W. J., Photothermally Triggered Cytosolic Drug Delivery via Endosome Disruption Using a Functionalized Reduced Graphene Oxide. *ACS Nano* **2013**, 7 (8), 6735-6746.
(26) Li, Y.; Hong, W.; Zhang, H.; Zhang, T.T.; Chen, Z.; Yuan, S.; Peng, P.; Xiao, M.; Xu, L. Photothermally triggered cytosolic drug delivery of glucose functionalized polydopamine nanoparticles in response to tumor microenvironment for the GLUT1-targeting chemo-phototherapy *J Control Release*. DOI:10.1016/j.jconrel.**2019**.11.031.
(27) Zimmerman, J. F.; Parameswaran, R.; Murray, G.; Wang, Y. C.; Burke, M.; Tian, B. Z., Cellular uptake and dynamics of unlabeled freestanding silicon nanowires. *Sci. Adv.* **2016**, 2 (12).
(28) Martin, C. R.; Kohli, P., The emerging field of nanotube biotechnology. *Nat. Rev. Drug Discov.* **2003**, 2 (1), 29-37.
(29) Tenne, R., Inorganic nanotubes and fullerene-like nanoparticles. *Nat. Nanotechnol.* **2006**, 1 (2), 103-111.
(30) Nan, A. J.; Bai, X.; Son, S. J.; Lee, S. B.; Ghandehari, H., Cellular uptake and cytotoxicity of silica nanotubes. *Nano Lett.* **2008**, 8 (8), 2150-2154.
(31) Kim, J. W.; Galanzha, E. I.; Shashkov, E. V.; Moon, H. M.; Zharov, V. P., Golden carbon nanotubes as multimodal photoacoustic and photothermal high-contrast molecular agents. *Nat. Nanotechnol.* 2**009**, 4 (10), 688-694.
(32) Bi, Y. P.; Lu, G. X., Controlled synthesis of pentagonal gold nanotubes at room temperature. *Nanotechnology* **2008**, 19 (27). 275306

(33) Sun, Y. G., Silver nanowires- unique templates for functional nanostructures. *Nanoscale* **2010**, 2 (9), 1626-1642.
(34) Sun, Y. G.; Mayers, B. T.; Xia, Y. N., Template-engaged replacement reaction: A one-step approach to the large-scale synthesis of metal nanostructures with hollow interiors. *Nano Lett.* **2002**, 2 (5), 481-485.
(35) Sieb, N. R.; Wu, N. C.; Majidi, E.; Kukreja, R.; Branda, N. R.; Gates, B. D., Hollow Metal Nanorods with Tunable Dimensions, Porosity, and Photonic Properties. *ACS Nano* **2009**, 3 (6), 1365-1372.
(36) Goodman, A. M.; Cao, Y.; Urban, C.; Neumann, O.; Ayala-Orozco, C.; Knight, M. W.; Joshi, A.; Nordlander, P.; Halas, N. J., The Surprising in Vivo Instability of Near-IR-Absorbing Hollow Au-Ag Nanoshells. *ACS Nano* **2014**, 8 (4), 3222-3231.
(37) Goris, B.; Polavarapu, L.; Bals, S.; Van Tendeloo, G.; Liz-Marzan, L. M., Monitoring Galvanic Replacement Through Three-Dimensional Morphological and Chemical Mapping. *Nano Lett.* **2014**, 14 (6), 3220-3226.
(38) Korte, K. E.; Skrabalak, S. E.; Xia, Y. N., Rapid synthesis of silver nanowires through a CuCl- or $CuCl_2$-mediated polyol process. *J. Mater. Chem.* 2008, 18 (4), 437-441.
(39) Gonzalez, E.; Arbiol, J.; Puntes, V. F., Carving at the Nanoscale: Sequential Galvanic Exchange and Kirkendall Growth at Room Temperature. *Science* **2011**, 334 (6061), 1377-1380.
(40) Sun, Y. G.; Xia, Y. N., Mechanistic study on the replacement reaction between silver nanostructures and chloroauric acid in aqueous medium. *J. Am. Chem. Soc.* **2004**, 126 (12), 3892-3901.
(41) Ye, X. C.; Jin, L. H.; Caglayan, H.; Chen, J.; Xing, G. Z.; Zheng, C.; Doan-Nguyen, V.; Kang, Y. J.; Engheta, N.; Kagan, C. R.; Murray, C. B., Improved Size-Tunable Synthesis of Monodisperse Gold Nanorods through the Use of Aromatic Additives. *ACS Nano* **2012**, 6 (3), 2804-2817.
(42) Vigderman, L.; Manna, P.; Zubarev, E. R., Quantitative Replacement of Cetyl Trimethylammonium Bromide by Cationic Thiol Ligands on the Surface of Gold Nanorods and Their Extremely Large Uptake by Cancer Cells. *Angew. Chem. Int. Ed.* **2012**, 51 (3), 636-641.
(43) Zhang, Y.; Newton, B.; Lewis, E.; Fu, P. P.; Kafoury, R.; Ray, P. C.; Yu, H. T., Cytotoxicity of organic surface coating agents used for nanoparticles synthesis and stability. *Toxicol. In Vitro* **2015**, 29 (4), 762-768.
(44) Chernova, T.; Sun, X. M.; Powley, I. R.; Galavotti, S.; Grosso, S.; Murphy, F. A.; Miles, G. J.; Cresswell, L.; Antonov, A. V.; Bennett, J.; Nakas, A.; Dinsdale, D.; Cain, K.; Bushell, M.; Willis, A. E.; MacFarlane, M., Molecular profiling reveals primary mesothelioma cell lines recapitulate human disease. *Cell death differ.* **2016**, 23 (7), 1152-1164.
(45) Carbone, M.; Ly, B. H.; Dodson, R. F.; Pagano, I.; Morris, P. T.; Dogan, U. A.; Gazdar, A. F.; Pass, H. I.; Yang, H. N., Malignant Mesothelioma: Facts, Myths, and Hypotheses. *J. Cell. Physiol.* **2012**, 227 (1), 44-58.
(46) Zimmerman, J. F.; Murray, G. F.; Tian, B. Z., Optical Determination of Silicon Nanowire Diameters for Intracellular Applications. *J. Phys. Chem. C* **2015**, 119 (52), 29105-29115.
(47) Behzadi, S.; Serpooshan, V.; Tao, W.; Hamaly, M. A.; Alkawareek, M. Y.; Dreaden, E. C.; Brown, D.; Alkilany, A. M.; Farokhzad, O. C.; Mahmoudi, M., Cellular uptake of nanoparticles: journey inside the cell. *Chem. Soc. Rev.* **2017**, 46 (14), 4218-4244.
(48) Mosquera, J.; Garcia, I.; Liz-Marzan, L. M., Cellular Uptake of Nanoparticles versus Small Molecules: A Matter of Size. *Acc. Chem. Res.* **2018**, 51 (9), 2305-2313.

(49) Jaque, D.; Maestro, L. M.; del Rosal, B.; Haro-Gonzalez, P.; Benayas, A.; Plaza, J. L.; Rodriguez, E. M.; Sole, J. G., Nanoparticles for photothermal therapies. *Nanoscale* **2014**, 6 (16), 9494-9530.
(50) Hunyadi, S. E.; Murphy, C. J., Bimetallic silver-gold nanowires: fabrication and use in surface-enhanced Raman scattering. *J. Mater. Chem.* **2006**, 16 (40), 3929-3935.
(51) Rintoul, R. C.; Rassl, D. M.; Gittins, J.; Marciniak, S. J.; Mesoban, K. C., MesobanK UK: an international mesothelioma bioresource. *Thorax* **2016**, 71 (4), 380-382.
(52) Booth, D. G.; Beckett, A. J.; Molina, O.; Samejima, I.; Masumoto, H.; Kouprina, N.; Larionov, V.; Prior, I. A.; Earnshaw, W. C., 3D-CLEM Reveals that a Major Portion of Mitotic Chromosomes Is Not Chromatin. *Mol. Cell* **2016**, 64 (4), 790-802.

Supporting Information

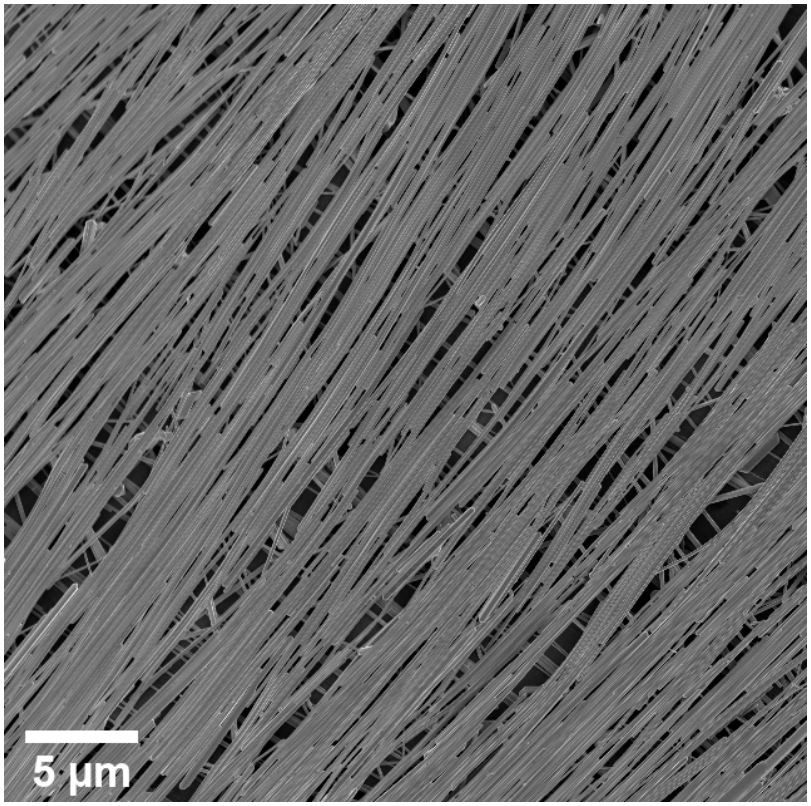

Figure S1 Wide-view SEM image of Ag NWs

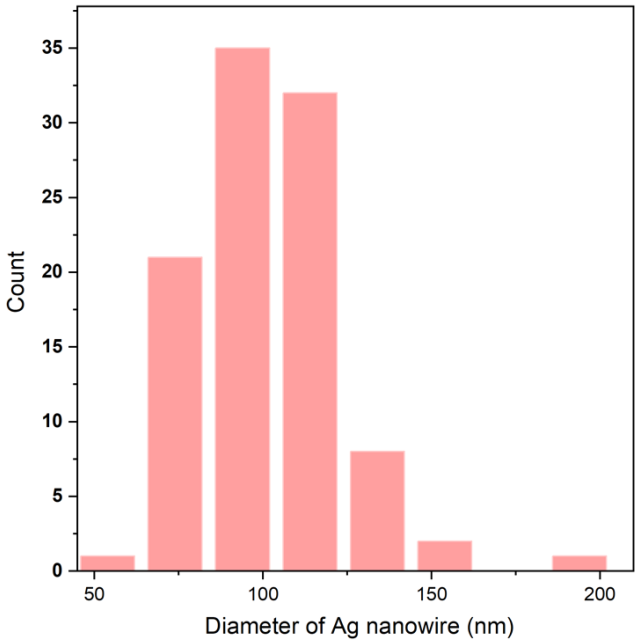

Figure S2 Diameter distribution of the Ag nanowires (100 nanowires were counted.)

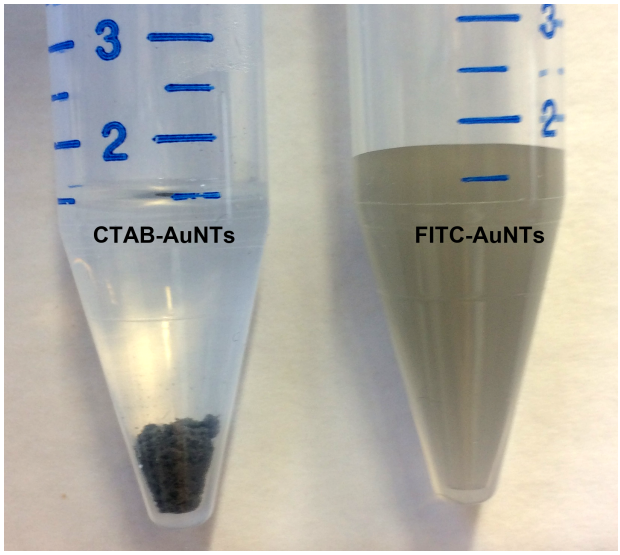

Figure S3 Digital image of CTAB-AuNTs and FITC-AuNTs in Milli-Q after 18 hour storage

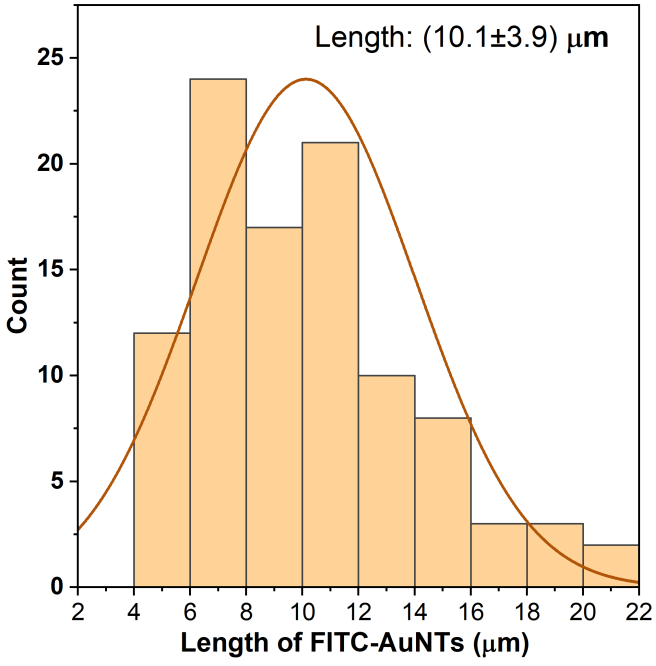

Figure S4 Length distribution of AuNTs (n=100)

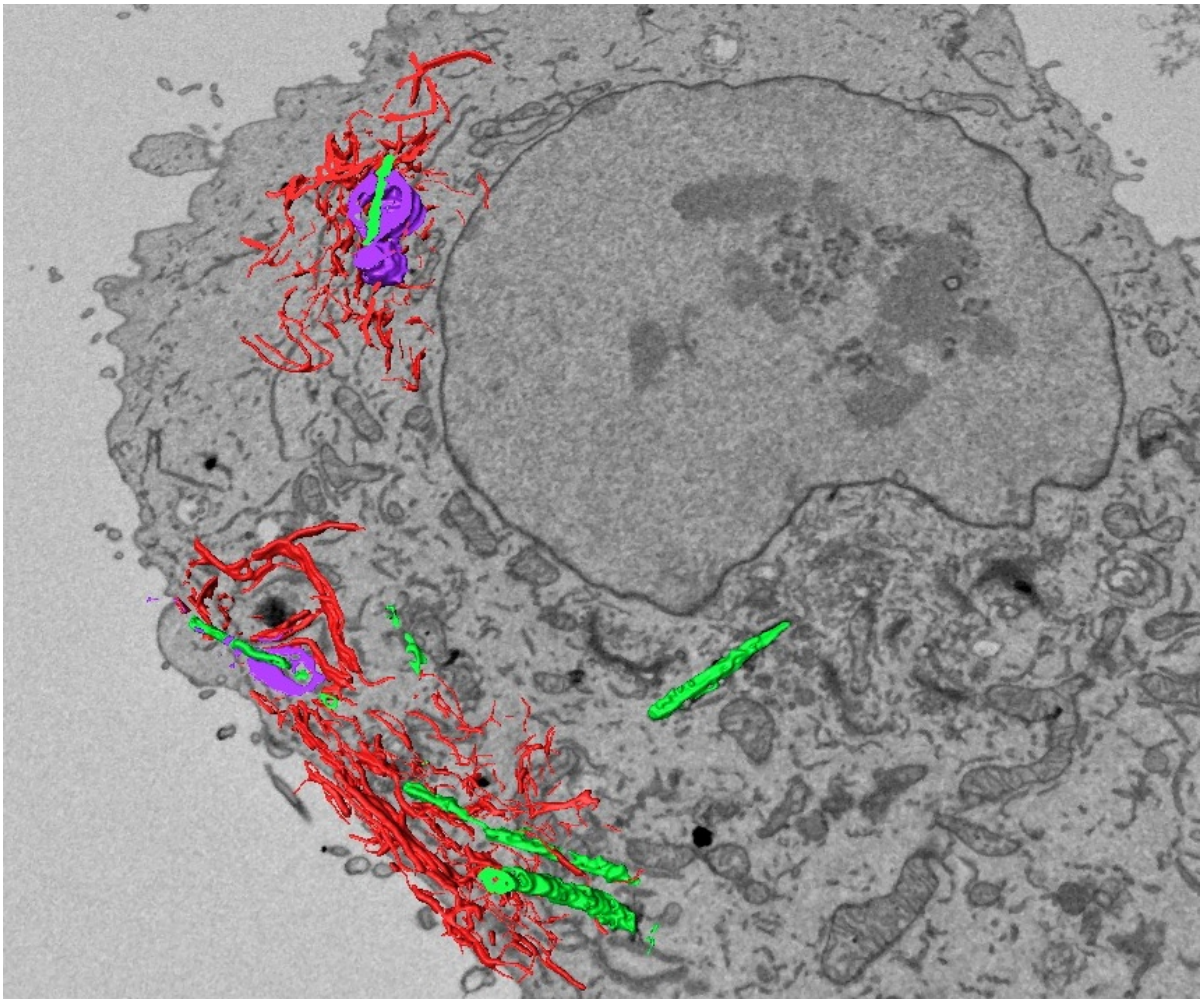

Figure S5 3D CLEM volume rendered structures demonstrating mixed distribution of AuNTs at 6 hours in mesothelioma cells (ER, red; AuNT, green; vesicles, magenta).

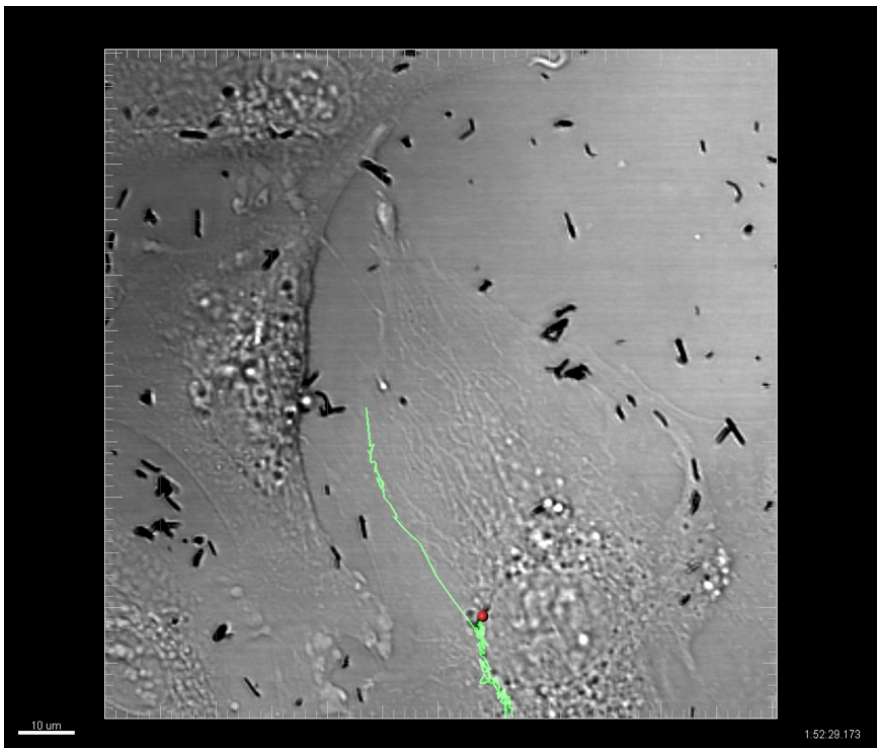

Video S1 Real-time visualisation of AuNT track: 101.

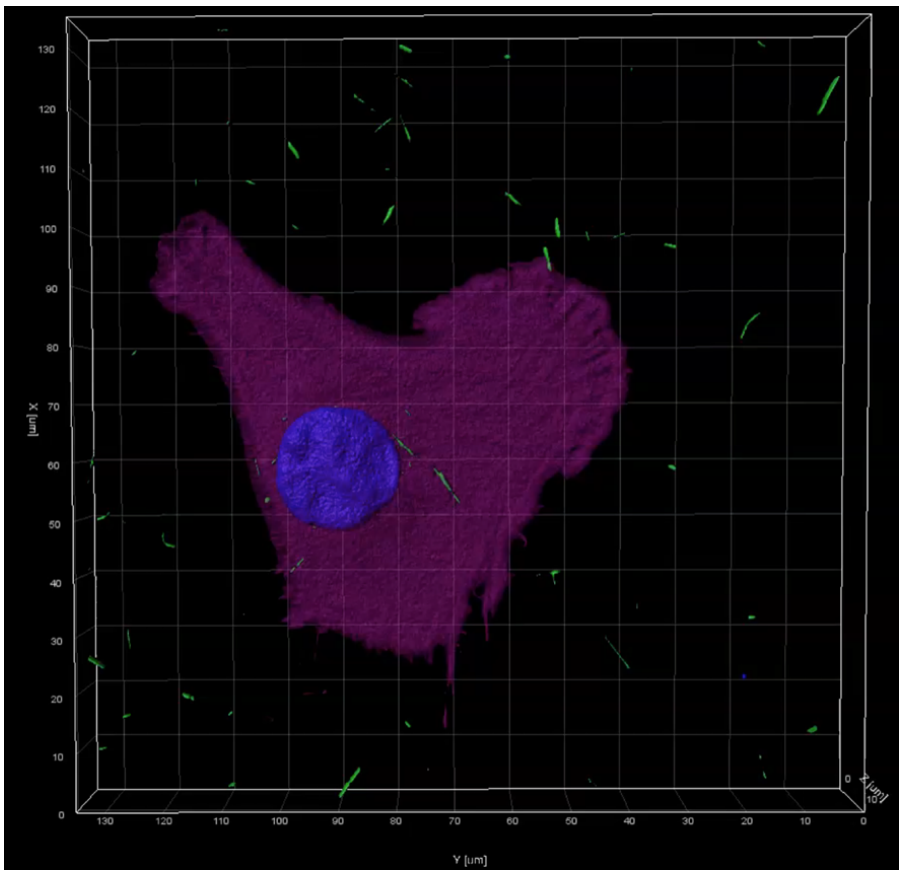

Video S2 AuNT uptake in MESO-7T cell rendered Imaris 9.1

	Cell diameter (μm)
1	54
2	121.2
3	114
4	109.2
5	111.6
6	112.8
7	73.2
8	73.2
9	99.6
10	132
11	120
12	111.6
13	110.4
14	74.4
15	97.2
16	121.2
17	85.2
18	120
19	97.2
20	52.8
Average	**99.54**
SD	**± 22.59**

Table S1 Average MESO-7T cell diameter (longest plane diameter measured).